Article

A Comparison between Local and Global Spaceborne Chlorophyll Indices in the St. Lawrence Estuary

Martin A. Montes-Hugo [1],*, Luca Fiorani [2], Salvatore Marullo [2], Suzanne Roy [1], Jean-Pierre Gagné [1], Rodolfo Borelli [2], Serge Demers [1] and Antonio Palucci [2]

[1] Institut de Sciences de la Mer de Rimouski, Université du Québec a Rimouski, 310 Alleé des Ursulines, Office P-216, Rimouski, QC G5L 3A1, Canada; E-Mails: suzanne_roy@uqar.qc.ca (S.R.); jean-pierre_gagne@uqar.qc.ca (J.-P.G.); serge_demers@uqar.ca (S.D.)

[2] Diagnostics and Metrology Laboratory (UTAPRAD-DIM), Italian National Agency for New Technologies, Energy and Sustainable Economic Development (ENEA), 00044 Frascati (RM), Italy; E-Mails: luca.fiorani@enea.it (L.F.); salvatore.marullo@enea.it (S.M.); rodolfo.borelli@enea.it (R.B.); antonio.palucci@enea.it (A.P.)

* Author to whom correspondence should be addressed; E-Mail: martinalejandro_montes@uqar.qc.ca; Tel.: +1-418-723-1986; Fax: +1-418-724-1842.

Abstract: Spaceborne chlorophyll indices based on red fluorescence (wavelength = 680 nm) and water leaving radiance (L_w) in the visible spectrum (*i.e.*, 400–700 nm) were evaluated in the St Lawrence Estuary (SLE) during September of 2011. Relationships between chlorophyll concentration (chl) and fluorescence were constructed based on fluorescence line height (FLH) measurements derived from a compact laser-based spectrofluorometer developed by ENEA (CASPER) and using spectral bands corresponding to the satellite sensor MERIS (MEdium Resolution Imaging Spectrometer). Chlorophyll concentration as estimated from CASPER (chl^{CASPER}) was relatively high NE of the MTZ (upper Estuary), and nearby areas influenced by fronts or freshwater plumes derived from secondary rivers (lower estuary). These findings agree with historical shipboard measurements. In general, global chl products calculated from L_w had large biases (up to 27-fold overestimation and 50-fold underestimation) with respect to chl^{CASPER} values. This was attributed to the smaller interference of detritus (mineral + organic non-living particulates) and chromophoric dissolved organic matter on chl^{CASPER} estimates. We encourage the use of spectrofluorometry for developing and validating remote sensing models of chl in SLE waters and other coastal environments characterized by relatively low to moderate (<10 g·m^{-3}) concentrations of detritus.

1. Introduction

The analysis of phytoplankton distribution in estuarine systems is of fundamental interest for planning human activities linked to recreation and managing ecological services such as shellfish farms. In fact, spatial and temporal patterns of phytoplankton can be used for identifying biological productive zones or detecting harmful microalgae blooms [1,2]. Chlorophyll concentration (chl) determinations are commonly used in oceanography for inferring temporal and spatial patterns of phytoplankton abundance. Unfortunately, mapping of chl may be challenging in large coastal environments due to the limitations associated with shipboard sampling (e.g., cruising cost, incomplete area coverage, low time-space resolution) and the lack of accurate remote sensing models for estimating phytoplankton pigments in waters having a terrestrial influence and optical properties dominated by chromophoric dissolved organic matter (CDOM) and/or detritus (organic + mineral) [3,4].

In general, there are two main types of ocean color models for estimating chl: (I). a_{ph}-based [5], where a_{ph} is the light absorption coefficient of phytoplankton (Table 1), and (II). fluorescence-based [6]. In both cases, the contribution of phytoplankton to the total water leaving radiance reaching the remote sensing sensor is directly associated to variations in chl. In general, the use of model type I is inaccurate and sometimes useless in optically complex waters due to the spectral overlap between phytoplankton and other dominant constituents affecting light attenuation (e.g., sediments, CDOM) [3,4,7]. Conversely, ocean color algorithms relying on chlorophyll-derived fluorescence signatures are less influenced by the presence of optical components having a strong light absorption (e.g., CDOM) or scattering (e.g., detritus) at the Soret bands [8–10].

The Saint Lawrence Estuary (SLE) is one the largest estuarine systems of the world (surface area = 12,850 km^2), and is characterized by waters having low visibility due to the presence of CDOM and particles in suspension [7,11]. In general, the inorganic fraction of SPM in the SLE is above 50% (range = 45 to 95%) [7] and presents the highest values upstream (e.g., over the MTZ) [12].

These characteristics make difficult the mapping of chl in this environment due to the high cost of field surveys and the large uncertainty of existing spaceborne models of chlorophyll [13]. Therefore, the main objective of the present study is to develop a low cost methodology that can be used to obtain synoptic and more accurate chl estimates in the SLE. To achieve this goal we propose a satellite-based approach using red fluorescence (wavelength = 680 nm) information and an optical model validated with CASPER (Compact and Advanced laser SPEctrometeR) measurements. In the first part of the study, we performed experiments using phytoplankton cultures and field samples in order to construct an empirical relationship between CASPER-derived fluorescence line height (FLH) and chl determinations. In the second part, we combined the CASPER-based parameterization and satellite ocean color observations for describing spatial patterns of chl in the SLE as a function of latitude and longitude. In addition, we compared these distributions with those derived from shipboard surveys, and three standard chl products proposed by ESA (European Space Agency) and NASA (National Aeronautics and Space Administration). Lastly, we quantified the relative bias on current NASA and

ESA spaceborne chl algorithms based on water leaving radiance (L_w) with respect to those estimates obtained from the CASPER-derived model.

Table 1. List of Acronyms.

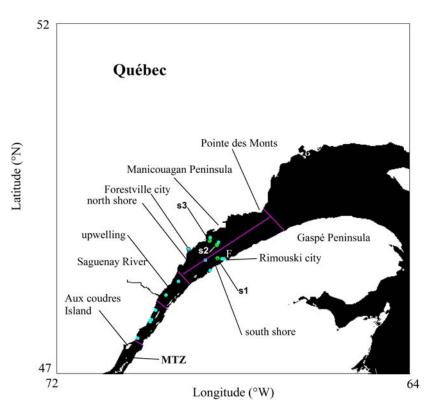| Abbreviation	Definition	Units
L_w	water leaving radiance	$mW \cdot cm^{-2} \cdot \mu m^{-1} \cdot sr^{-1}$
nL_w	Normalized L_w or L_w assuming sun at zenith and no atmosphere	$mW \cdot cm^{-2} \cdot \mu m^{-1} \cdot sr^{-1}$
R_{rs}	Remote sensing reflectance	sr^{-1}
FLH	Fluorescence line height	$mW \cdot cm^{-2} \cdot \mu m^{-1} \cdot sr^{-1}$
FLH^{CM}	Raman-normalized FLH as derived from CASPER	$mW \cdot cm^{-2} \cdot \mu m^{-1} \cdot sr^{-1}$
nFLH	Normalized FLH or FLH computed using nL_w	$mW \cdot cm^{-2} \cdot \mu m^{-1} \cdot sr^{-1}$
a_{ph}	Light absorption coefficient of phytoplankton	m^{-1}
ΦF	Quantum yield of fluorescence	dimensionless
chl^{SM}	Chlorophyll concentration as derived from ship and MODIS measurements	$mg \cdot m^{-3}$
chl^{CASPER}	Chlorophyll concentration as derived from MERIS data and CASPER-derived FLH relationship	$mg \cdot m^{-3}$
chl^{oc3}	Chlorophyll concentration computed using the oc3 model	$mg \cdot m^{-3}$
chl^{GSM}	Chlorophyll concentration computed using the Garver-Siegel-Maritorena model	$mg \cdot m^{-3}$
chl^{NN}	Chlorophyll concentration computed using the neural network model	$mg \cdot m^{-3}$
CDOM	Chromophoric dissolved organic matter	m^{-1}
CDM	CDOM absorption coefficient at 443 nm	m^{-1}
TSM	total suspended matter concentration	$g \cdot m^{-3}$
MTZ	Maximum turbidity zone	

2. Materials and Methods

2.1. Field Surveys

Two experiments were designed in the SLE for relating *in situ* chl determinations with satellite- and CASPER-derived fluorescence measurements. In the first experiment, water samples for chl were obtained from surface waters (0–20 m depth) of different sections of the Estuary as part of an oceanographic cruise on the Coriolis II vessel and organized by ISMER during 17–22 September 2011 (Figure 1). The chosen sampling depth interval is larger than the maximum depth range contributing to the fluorescence signal detected at the surface of SLE waters. However, due to the strong vertical mixing of SLE waters [14], magnitude of fluorescence or chl is quite homogeneous in the top 20 m of the water column. Thus, no fluorescence variations due to vertical layering of chl are anticipated in this study.

Discrete sample volumes (0.5 to 1 L) for chl measurements were collected at three depths (5, 10 and 20 m) using Niskin bottles attached to an oceanographic rosette. Vertical profiles were performed in 23 locations encompassing waters west of Rimouski city (48°26'N, 68°31'W) and east of Aux-Coudres Island (47°24'N, 70°22'W). Since some sampling stations were revisited on different days, a smaller number of sampling positions are shown in Figure 1. In the second experiment, we performed a time series of chl and CASPER fluorescence measurements in the lower estuary (hereafter 'Frascati' station, 48.483°N, 68.533°W) (Figure 1). This site was chosen near (~5 km) the port of Rimouski city where a temporary lab was assembled to facilitate processing of samples. We used a small boat (7 m

length) for collecting surface water samples (*i.e.*, 3 m depth) during the morning (9:00 am and 11:00 am), noon (12:00 pm) and afternoon (13:30 pm and 14:45 pm) of 9 September 2011.

Figure 1. Study area. Ship stations (solid circles), time series at Frascati station (F). The mouth of the estuary begins at Pointe des Monts. The upper estuary extends SW of Saguenay River entrance. Boundaries between SLE regions (magenta lines), MTZ is maximum turbidity zone, s1, s2, and s3 correspond with satellite match-ups during the September 2011 cruise.

2.2. Lab Analysis of Optical Variables

Discrete fluorometric determinations of chl were performed following the acidification technique [15]. Briefly, each volume of sample (100 and 500 mL) was concentrated using a fiber glass filter (GF/F, Whatmann, mean pore diameter = 0.7 microns). Then, organic-soluble pigments were extracted with 90% acetone during 24 h. The fluorescence before and after the addition of diluted acid (HCl 5%) was measured at room temperature (25 °C) and using a single excitation-emission wavelength (λ_{exc} = 443 nm, λ_{emiss} = 680 nm) fluorometer RD-10AU (Turner designs).

The fluorescence emission spectra of water samples were measured within the size range 0.2-30 microns using the laser-based fluorometer CASPER [16]. This instrument was originally designed to study desertification and includes the following innovations: (1) it is a portable optical system that can be operated by only one person, (2) it has two laser sources one in the UV (wavelength = λ = 266 nm, 2 mW) and one in the visible spectrum (λ = 405 nm, power = 25 mW), that make possible simultaneous measurements of multiple optical components (e.g., CDOM and chl), (3) it allows discrimination between dissolved and particulate phases due to two sets of filters, one to eliminate particulates above 30 μm (Millipore optiscale capsule, polycarbonate, pore size = 30 μm, diameter = 69 mm), and another one to separate fractions below and above 0.2 μm (Sartorius,

Sartobran P, mixed cellulose esters, pore size = 0.2 μm, diameter = 47 mm), (4) it provides fast determinations since each sample (particulate + dissolved) can be analyzed in less than one minute, and (5) it has a miniature detector consisting of a fiber optic spectrometer (USB2000+, 2,048 pixels, 200–1,100 nm, Ocean Optics).

Each measurement requires five steps: (1) purge and fill up of system components (tygon tubing and quartz cuvettes) with water samples, (2) background light measurement for each excitation wavelength by alternatively turning off the lasers, (3) high spectral resolution (0.3 nm) fluorescence spectra measurements at UV excitation, (4) idem as (3) but using the visible wavelength, and (5) rinsing of system components with deionized water (Milli-Q). The minimum detection level of CASPER for measuring chlorophyll is 0.1 $\mu g \cdot L^{-1}$ at an emission wavelength of 680 nm.

2.3. Relationships between FLH and Chlorophyll

Chlorophyll-fluorescence is a major pathway for dissipating energy in excess going to photosystem II or PS II (*i.e.*, the main protein complex of photosynthesis). The ratio fluorescence/chlorophyll is variable and depends on light harvesting pigments or antenna characteristics and rate of electron flow between PS II and PS I [17]. Fluorescence/chlorophyll increases with light as reaction centers become saturated and starts decreasing beyond saturating light intensities as absorbed photons are transformed into heat due to the xanthophyll cycle. In Canadian coastal waters, Neville and Gower [18] showed for the first time a positive correlation between chlorophyll *a* concentration and the magnitude of sun-stimulated fluorescence at 685 nm as estimated from airborne reflectance spectra. Based on these preliminary results, Borstad *et al.* [19] suggested the use of FLH for estimating chl even though there is a large variability of FLH/chl (0.01 to 0.08 $mW \cdot cm^{-2} \cdot sr^{-1} \cdot \mu m^{-1} \cdot mg \cdot Chlorophyll^{-1}$) between different water types. In simple terms, FLH is defined as follows:

$$FLH = L_F - kL_S - (1 - k) L_L \qquad (1)$$

$$k = (\lambda_L - \lambda_F) (\lambda_L - \lambda_S)^{-1} \qquad (2)$$

where L_F, L_S and L_L are the radiance measurements coinciding with the chlorophyll fluorescence peak (L_F) and spectral limits (lower, L_S and higher, L_L) defining FLH, and λ_S, λ_F and λ_L are the corresponding wavelengths. The linear baseline between L_S and L_L is weakly influenced by atmospheric components such as oxygen and water vapor [10,20], and other optical components when waters are classified as case I (*i.e.*, phytoplankton covaries with other optical components) [9,10]. Thus, most of the variability of FLH in oceanic waters can be attributed to phytoplankton abundance and physiology [9,10,20]. However, in case II waters, the use of FLH for estimating chl may be questionable or useless depending on the contribution of CDOM and detritus to the light attenuation in the fluorescence excitation and emission spectral ranges [9].

Response of FLH to different chl values was analyzed based on Raman-normalized (wavelength = 468 nm) CASPER spectra (hereafter FLH^{CM}). Raman normalization is intended to eliminate CASPER fluorescence variability due to changes in light source intensity or water temperature. FLH^{CM} was computed based on MERIS (MEdium Resolution Imaging Spectrometer) radiometric channels along with their respective bandwidths ($L_S = 665 \pm 10$ nm, $L_F = 681 \pm 7.5$ nm, and $L_L = 709 \pm 10$ nm). Unlike MODIS (Moderate Resolution Imaging Spectroradiometer), spectral

location of radiometric channels in MERIS is more suitable for chlorophyll fluorescence in terms of signal/noise ratio (1.4 fold higher) [20]. In addition, the use of FLH instead of single wavelength (e.g., centered at 680 nm) chl indices is justified by the fact that remotely sensed (airborne or spaceborne) FLH calculation minimizes elastic scattering contribution originated from water and atmospheric components [10,20].

Samples for FLH-chl experiments were obtained during a time series performed at the Frascati station (see Section 2.1), and from phytoplankton lab cultures. For the second comparison, we prepared four chl dilutions (8.2, 28.7, 64.8 and 309.3 mg·m^{-3}) from the same culture of microalgae *Nannochloropsis oculata*. This Eustigmatophyceae species was cultivated using f/2 medium and samples were collected during the exponential phase of growth.

2.4. Satellite Ocean Color Measurements

The analysis of spaceborne ocean color information allowed us to investigate three main questions: (1) How do satellite chl estimates based on CASPER-chl relationships compare with global ocean color products or local parameterizations developed using concurrent ship and satellite-derived fluorescence data?, (2) What is the influence of CDOM and detritus on chl estimates computed from FLH measurements?, and (3) How alike are regional spatial patterns of fluorescence- *vs.* L_w-based chl in the SLE?

2.4.1. Datasets

Global ocean color products derived from SeaWiFS (Sea-viewing Wide Field-of-view Sensor), MODIS-Aqua, MERIS sensors were browsed from NASA [21] and ESA [22] data distribution servers, and with a spatial resolution of 4.5 and 5.6 km, respectively. The analysis of satellite measurements was performed using two images (1 MERIS and 1 MODIS-Aqua) obtained during 28 September 2011. Redundant information was avoided by selecting complementary ocean color products from NASA (normalized FLH or nFLH, chlorophyll band-ratio model oc3 or chl^{oc3}) and ESA (CDOM absorption coefficient at 443 nm or CDM, total suspended matter concentration or TSM, nL_w or normalized L_w, chlorophyll neural network model or chl^{NN}, and chlorophyll band-ratio model Garver-Siegel-Maritorena or chl^{GSM}).

All the online chlorophyll products used in this study are based on L_w even though they differ with respect to: (1) the mathematical model (chl^{oc3} is empirical, chl^{GSM} is semi-empirical, chl^{NN} is statistical), and (2) the spectral information (3 wavelengths in chl^{oc3} *vs.* 4 or more in chl^{GSM} or chl^{NN}). The inversion model chl^{oc3} is based on a polynomial of order four that depends on the maximum remote sensing reflectance (R_{rs}) blue-green band ratio (*i.e.*, $R_{rs}(443)/R_{rs}(551)$ *vs.* $R_{rs}(488)/R_{rs}(551)$) [23]. The chl^{GSM} model computes chl by minimizing differences between spectral nL_w measurements at four or more wavelengths in the visible range and simulated nL_w derived from a quadratic function [24]. The solution is found by optimizing the specific a_{ph} (*i.e.*, $a_{ph}* = a_{ph}/chl$), the spectral slope of particulate backscattering and absorption coefficient of CDOM using a nonlinear least squares technique. Notice that the optimization of the spectral slope of particulate backscattering may have implicit a major error due to the inherent uncertainties associated with the backscattering measurements from the space.

Lastly, the chl^{NN}, originally named chl2, is obtained from a_{ph} at 443 nm after training a neural network using spectral nL_w corresponding to 8 MERIS bands in the visible spectrum [25]. Briefly, nL_w, downwelling irradiance, and R_{rs} are simulated for different solar and viewing angles with a Monte Carlo radiative transfer model that is initialized with chl (1–50 mg·m^{-3}), CDM (0.1–2 m^{-1}), and TSM (1–50 g m^{-3}) values obtained from the North Sea and Baltic Sea waters [26]. The neural network is a feed-forward back-propagation optimization technique composed by two hidden layers of neurons and four output variables (chl^{NN}, CDM, TSM, and aerosol path radiance at 670 nm).

2.4.2. Analysis of Imagery

The selection of images was based on the following criteria: (1) each swath should have at least an area covered with 25% of valid pixels, (2) match-ups between satellite-derived nFLH measurements and shipboard samples should occur within 3-h of satellite overpass, and (3) the time window for the satellite overpass should correspond with September 2011, a period of the year characterized by minimum cloudiness. Quality control for each pixel bin was based on latest flags suggested by NASA and ESA and mainly related to land, bottom, turbidity and glint. In addition, NASA L2 flags (N = 32) are more with respect to ESA flags (N = 16) because the latest summarizes many of the former in bits 13 to 15. For each ocean color product, we defined a valid pixel as a pixel that has not been flagged by the previous constraints and has no negative values since they may reflect inversion model issues or very low signal/noise ratios caused by dominance of water constituents such as CDOM.

Two types of satellite-derived chl indices based on fluorescence were used, one derived from MODIS-Aqua nFLH values (hereafter, chl^{SM}), and another one based on CASPER model and nFLH computed from MERIS nL_w measurements (hereafter chl^{CASPER}). In all cases, negative nFLH or nL_w values were excluded from the analysis, and unlike other studies [27] no offsets were used to initialize nFLH when chl is 0 mg·m^{-3} since these corrections are small compared the detection limit of L_F (±0.002 mW·cm^{-2}·sr^{-1}·µm^{-1}) (Equation (7) in [10]), and the fact that our chl proxies are not totally absolute because of the lack of field validation. Unlike L_w, nL_w is corrected by the sun-sensor geometry as well as for atmospheric scattering and absorption [28].

Calculation of chl^{CASPER} was performed using FLH^{CM}-chl functionality derived in the lab and consisting in field and phytoplankton culture samples. Unfortunately, no quasi-simultaneous comparisons between *in situ* FLH^{CM} and MERIS imagery data were available in this study. Thus, we propose an algorithm that only relies on lab optical measurements. We recognize two main differences for applying this chl proxy: (1) the spectral characteristics of the excitation light source in CASPER (*i.e.*, laser-based and monochromatic) with respect to MERIS (sun-induced and multiple wavelengths), and (2) variations between CASPER and MERIS detector response functions. These variations, however, may be disregarded here if the main purpose is to perform relative comparisons in terms of chl spatial trends or inter-algorithm comparisons.

Processing of satellite ocean color products derived from NASA and ESA were performed with the development platform BEAM 4.10.3 [29] and the Windows Image Manager [30] software, respectively. Image data was extracted using a filter of 3 × 3 pixels and was intended to relate ship and spaceborne information, compare nFLH-based variables with global ocean color products of chl, and evaluate interference of CDOM and detritus on nFLH in different regions of the SLE.

2.4.3. Statistical Analysis

Variation of chl as a function of FLH^{CM} was quantified for *in situ* and cultivated phytoplankton samples using a linear regression model type II (*i.e.*, random error for dependent and independent variables) based on least squares differences [31]. Similarity between chl^{CASPER} (independent variable x), chl^{SM}, and global ocean color products of chl (dependent variable y) was evaluated based on magnitude of coefficient of determination (r^2) corresponding to a polynomial regression function: y = mx + I, where m and I are the slope and the intercept, respectively. For pigment concentrations above 0.5 mg·m^{-3}, the phytoplankton fluorescence has a non-linear behavior as a function of chl due to a greater re-absorption of photons [20]. Thus, we also examined the response of chl^{SM} and global chl products with respect to chl^{CASPER} variations by fitting the data using a hyperbolic model: y = (k1 x)/(k2 + x), where x is chl^{CASPER} and k1 and k2 are constants that are computed by the Levenberg-Marquardt non-linear least square differences method. Discrimination and removal of outliers affecting the aforementioned functionalities was conducted by applying a Hampel filter [32].

Ratios between chl^{oc3}, chl^{GSM} or chl^{NN} (numerator), and chl^{CASPER} (denominator) were computed for each pixel bin and used to examine the relative bias between the fluorescence-based and the L_w-based chl indices. The lower the magnitude of r^2 and the greater the (m-1) difference the larger the relative error of chl estimates as computed using the respective global ocean color algorithm. The potential interference of CDOM and detritus on nFLH and consequently chl^{CASPER} was explored for each SLE sub-region (Figure 1) based on linear regression models type II between nFLH and CDM, and nFLH and TSM, respectively. Notice that TSM is used here as a proxy for detritus concentration since more than 50% of the TSM mass in the SLE is composed by inorganic matter [7], however this parameter also includes a variable contribution of microalgae that may have a substantial contribution to the fluorescence signal. CDOM will mainly compete with light absorption by chlorophyll at relatively short wavelengths (*i.e.*, <400 nm) [9,20], thus less red fluorescence is anticipated in those cases where CDOM is a dominant water optical component. This effect is expected to occur if the slope of the nFLH-CDM regression is less than zero. Moreover and over detritus-rich waters, most of the reflected energy in the spectral range 670–690 nm is associated to elastic scattering contributions coming from sediments and/or organic non-living particulates. Thus, as TSM becomes enriched in detritus, nFLH is not longer a good indicator of chl [33] and an uncoupling between nFLH and TSM is anticipated resulting in m's that are near zero or negative.
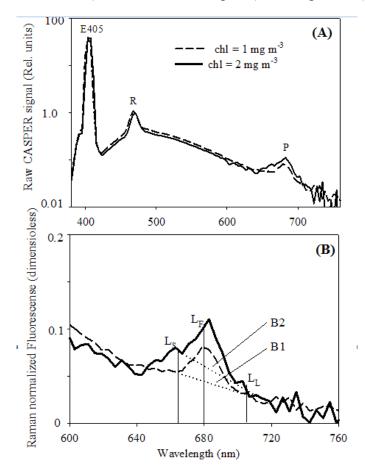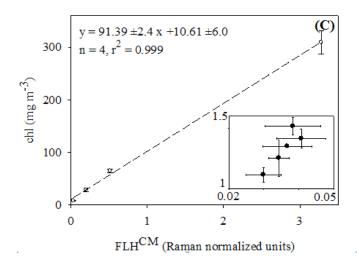
3. Results

3.1. Relationships between chl and FLH as Derived from Field and Lab Samples

The raw and processed fluorescence signal as measured by the CASPER spectrofluorometer and corresponding to samples obtained during the Frascati time series is shown in Figure 2(A,B). As expected, variability of the raw CASPER emission spectra (*i.e.*, non-corrected by elastic contributions from the excitation source and inelastic water contributions from Raman) in the spectral range 380–760 was mainly attributed to changes in phytoplankton pigments when chl values varied between 1 and 2 mg·m^{-3} (Figure 2(A)). In fact, signal modifications due to the laser source performance (18.2% at λ = 405 nm) or water temperature variability (13.8% at λ = 468 nm) was small with respect to

phytoplankton-related fluorescence (41.5% at λ = 680 nm). In addition, it is worthy to emphasize the spectral shift of the emission peak of chlorophyll (~4 nm) to longer wavelengths when chl was doubled (Figure 2(B)). The relationship between chl and FLH^{CM} measurements based on *in situ* measurements or phytoplankton culture samples was linear for a chlorophyll concentration range between 1.1 and 309.3 mg·m^{-3} (Figure 2(C)). Regression slope coefficients were different from zero for both functionalities; however the magnitude of *m* for CASPER and Turner comparisons based on phytoplankton samples growing in controlled conditions was 2.7-fold greater (*i.e.*, the fluorescence per unit of chl was 2.7-fold smaller) with respect to that computed using field samples (chl = FLH^{CM} (33.4 ± 9.3) + 0.13 ± 0.34, r^2 = 0.81, N = 5).

Figure 2. CASPER fluorescence emission spectra and relationships with chl. (**A**) Raw spectra examples for 1 (broken line) and 2 (solid line) mg·m^{-3} of chlorophyll, Raman emission (R), chlorophyll excitation (E405) and emission (P) peaks, B1 and B2 are the fluorescence baselines for chl of 1 and 2 mg·m^{-3}, respectively; (**B**) idem as a) but Raman-normalized spectra, L$_F$, L$_S$ and L$_L$ are explained in Section 2.3, (**C**) chl as a function of FLH^{CM} based on phytoplankton cultures samples (empty circles), error bars correspond to two standard errors (se), linear regression curve (--), coefficients ± 2 se (left-upper corner). Relationship between chl (mg·m^{-3}, vertical axis) and FLH^{CM} (dimensionless, horizontal axis) based on field samples (lower-right inset).

Figure 2. *Cont.*

Since our intention here is to propose a fluorescence-based index and not an absolute metrics of chl that can be applied to optical satellite measurements over the SLE, and given the limited range of pigment values used when comparing field samples, we decided to use the chl-FLH^{CM} function obtained from phytoplankton cultures for modeling spaceborne chl based on fluorescence line height estimates.

3.2. Chlorophyll Proxies Based on Satellite-Derived FLH and L_w

The direct relationship between *in situ* chl and satellite fluorescence was supported by shipboard surveys performed during 21 September 2011 (Figure 3). Given the range of pigment concentrations measured during the cruise (0.2 to 5.8 mg·m^{-3}), a non-linear variation should be expected between averaged surface (0–20 m depth) chl determinations and MODIS-Aqua nFLH values. However, this effect could not be detected since only 3 of 23 cruise stations coincided in time and space with satellite measurements. The resulting linear regression function was developed with samples obtained across the lower estuary, had a regression slope greater than 1 ($P < 0.05$), and was characterized by a regression intercept not different from zero ($P > 0.05$). Despite the small time difference between MODIS-Aqua (17:10 GMT) and MERIS (16:53 GMT) overpasses during 28 September 2011, the linear covariation between chl^{SM} and chl^{CASPER} was relatively weak ($r^2 = 0.335$) (Figure 4(A)). Nevertheless, the co-dependency between chl^{SM} and chl^{CASPER} values was greater with respect to that seen between CASPER and L_w-based chl indices (r^2 up to 0.255, Figure 4(C)). Notice that the number of valid data points differ between regression curves due to geographic differences in algorithm performance. In general and based on the regression slope, chl^{CASPER} was underestimated and overestimated with respect to chl^{SM} ($m > 1$, $P < 0.05$, Figure 4(A)) and chl^{NN} ($m < 1$, $P < 0.05$, Figure 4(D)), respectively. The regression intercept was in all cases greater than one but for chl^{CASPER} − chl^{SM} and chl^{CASPER} − chl^{oc3} where I was not different from zero ($P < 0.05$). The hyperbolic regression model only converged when chl^{CASPER} was related with chl^{GSM} and chl^{NN} (Figure 4(C,D); Table 2), and presented values of r^2 that reflected a slight improvement on explaining residual variability (up to 7%) with respect to the linear regression functions.

Figure 3. Correspondence between shipboard chlorophyll and satellite fluorescence. nFLH is computed based on MODIS-Aqua channels, the linear regression type II model (dash line, upper left corner), between parentheses one standard error, error bars for data points correspond to 2 standard errors. Location of s1, s2 and s3 sampling stations is indicated in Figure 1.
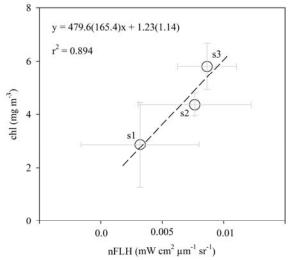

Figure 4. Relative bias of satellite-derived chl indices with respect to chl^{CASPER}. (**A**) shipboard empirical algorithm (chl^{SM}), (**B**) oc3, (**C**) Garver-Siegel-Maritorena, and (**D**) neural network model. Linear fitting (solid line) and model equation (right corner), two standard errors between parentheses, all plots in semi-$\log_{10}$ scale.
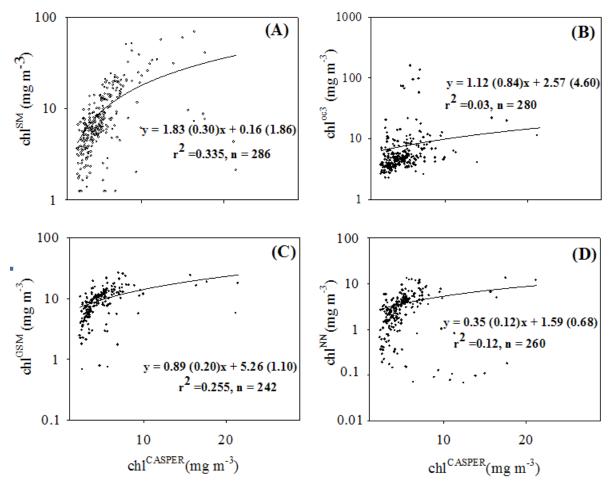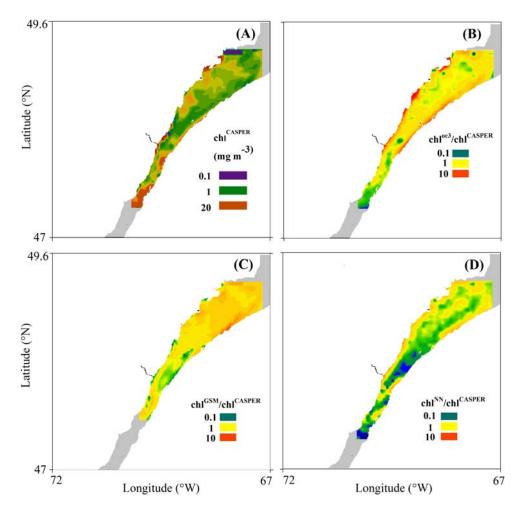
Table 2. Statistics summary of hyperbolic regressions between chl^{CASPER} and global products of chl. For each chl model, regression parameters k1 and k2 (first line) and their standard error (second line) are given. N is the number of observations, *statistically different from 0 at 95% confidence level ($P < 0.05$).

	k1	k2	r^2	N
chl^{SM}	109.3	51.81	0.35	286
	55.5	30.46		
chl^{oc3}	33.51	14.57	0.03	280
	28.80	17.50		
chl^{GSM}	27.85*	8.58*	0.37	242
	3.63	1.82		
chl^{NN}	9.99*	9.15*	0.18	260
	2.36	3.52		

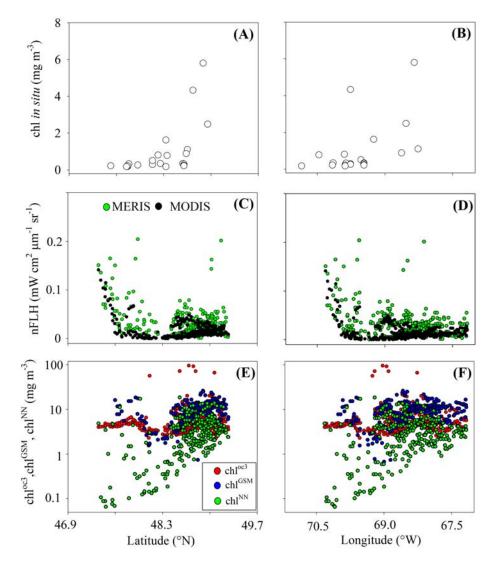*3.3. Spatial Coherence between Fluorescence and L_w-Based Indices of chl*

The spatial distribution chl^{CASPER} values throughout the SLE and during noon of September 28, 2011, was very irregular with values changing up to one order of magnitude (2.27–21.5 mg·m^{-3}) (Figure 5(A)). Highest pigment concentrations (>20 mg·m^{-3}) were found north of the MTZ and near the mouth of the most important north shore rivers draining in the lower part of the St Lawrence Estuary (Saguenay, Manicougan and Outardes). Intermediate to high values (1–10 mg·m^{-3}) were observed south of the Outardes Delta and over the main channel, and around the archipelago extending along the south shore of the lower estuary (Figure 1). These spatial patterns were also observed in satellite images collected 15 days before or after September 28 (data not shown). In general and consistent with Figure 4, the ratio between chl^{CASPER} and chl^{oc3}, chl^{GSM} and chl^{NN} over the whole SLE varied 134, 48 and 860-fold, respectively (Figure 5(B-D)). Lower chl^{oc3} values with respect to CASPER estimates were mainly computed in the upper estuary (ratio < 0.5) (Figure 5(B)). Conversely, oc3 pigment predictions overestimated CASPER (ratio > 20) over waters near the coast of the north and south shores of the lower estuary. In general, chl^{GSM} and chl^{CASPER} estimates followed comparable spatial patterns even though large differences were observed in specific locations of the south shore (ratios < 0.2) and waters north-east of Rimouski city (ratios > 5) (Figure 5(C)). Lastly, the spatial distribution of chl^{NN} showed relatively low values (ratio up to 0.005) with respect to chl^{CASPER} in a large portion of the Estuary including upper and lower sections, and mostly coinciding with deeper waters along the Laurentian Channel (Figure 5(D)).

Figure 5. Spatial distribution of relative bias between global ocean color products and CASPER-related proxy of chl. (**A**) CASPER-derived chl, (**B**) ratio between oc3 and CASPER models, (**C**) idem as (**B**) but for the Garver-Siegel-Maritorena model and (**D**) idem as (**B**) but for the neural network model. No data (grey), land (white), plots are in $\log_{10}$ scale.

These remarkable differences in chl indices may lead to ambiguous spatial patterns of phytoplankton along and across the Estuary. In fact, latitudinal and longitudinal changes in chlorophyll during the September 2011 cruise showed no increase toward the southwest, a trend clearly defined by MODIS-Aqua or MERIS fluorescence measurements (Figure 6(A–D)). Notice that these discrepancies were also present even after analyzing satellite scenes corresponding to other days during September. Differences in large scale spatial patterns were also striking between satellite fluorescence and global products of chl. In general, latitudinal and longitudinal distribution of chl^{oc3} magnitude was quite constant compared to those associated with satellite fluorescence (Figure 6(C–F)). Geographic variability of chl^{GSM} and satellite fluorescence was comparable even though this correspondence tended to disappear over the westernmost locations of the upper estuary (Figure 6(E)). Conversely, the chl^{NN} showed an inverse spatial variation with respect to nFLH, and consequently was a very misleading index for mapping phytoplankton distributions in the SLE (Figure 6(F)).

Figure 6. Spatial gradients of satellite-derived proxies of chl. (**A,B**) shipboard measurements, (**C,D**) satellite-based normalized fluorescence line height, and (**E,F**) L_w-based satellite products as a function of latitude (left panels) and longitude (right panels). Different symbols are used to discriminate sensors and chl models.
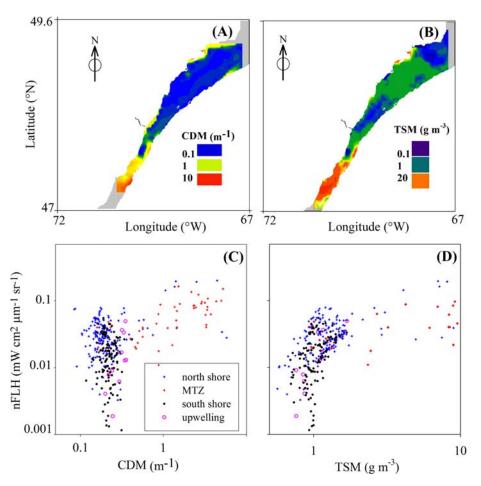

3.4. Effects of CDOM and Detritus on FLH

Relationships between satellite-derived nFLH, CDM, and TSM values during 28 September 2001 are shown in Figure 7. In general, CDM and TSM presented higher values over areas influenced by river discharge and turbidity plumes (e.g., NE of the MTZ in the upper estuary and along the north shore in the lower estuary) (Figure 7(A-B)). The highest concentrations of CDM (up to 5.7 m^{-1}, north shore) and TSM (up to 20 g·m^{-3}, MTZ) were found in the same sub-regions where maximum values of chl^{CASPER} (>20 mg·m^{-3}) and nFLH (up to 0.20 mW·cm^2·µm^{-1}·sr^{-1}) were obtained (Figure 5(A) and Figure 7(C,D)). Likewise, the lowest CDM (<0.1 m^{-1}) and TSM (<1 g·m^{-3}) values were detected in those locations characterized by the lowest chl^{CASPER} (<3 mg·m^{-3}) and nFLH (<0.005 mW·cm^2·µm^{-1}·sr^{-1}) values (e.g., central portion of lower estuary) (Figures 5(A) and 7(A,B)). In general, the magnitude of nFLH varied independently from CDOM variability when CDM magnitude was less than 0.3 m^{-1} (e.g., all sub-regions). Also, nFLH appeared to be positively

associated with CDOM at CDM values greater than 0.5 m^{-1} (e.g., north shore and MTZ) even though the slope of this trend was not different from zero ($P > 0.05$) (Figure 7(C)). Conversely, nFLH was positively related with TSM when TSM concentrations were relatively low (<2 g·m^{-3}) (all sub-regions, $r^2 = 0.20$, nFLH = 0.028 TSM (8·10^{-4}, 1 standard error) + 0.006 (9·10^{-4}), N = 4719, Figure 7(D)). Likewise, this correspondence was weaker at greater TSM values (2–10 g·m^{-3}), and disappeared at TSM greater than 10 g·m^{-3} when nFLH reached a relatively constant value around 0.1 mW·cm^2·μm^{-1}·sr^{-1}.

Figure 7. Response of MERIS-derived nFLH to CDOM and TSM changes. (**A**) light absorption coefficient of CDOM at 443 nm, (**B**) concentration of total suspended particulates, (**C**) normalized fluorescence line height as a function of CDM, and (**D**) idem as (**C**) but as a function of TSM. No data (grey), land (white), data points for each region of the SLE (Figure 1) are plotted in log$_{10}$ scale and indicated with different symbols.

4. Discussion

4.1. Relationships between chl and CASPER Fluorescence

Lab measurements using CASPER demonstrated that fluorescence emission at a wavelength of 680 nm varied less with respect to chlorophyll changes. Indeed at chl >0.5 mg·m^{-3}, a variation in chlorophyll of 100% only corresponded with a 42% relative variation of normalized fluorescence line height. At higher pigment concentrations (*i.e.*, chl > 0.5 mg·m^{-3}), light excitation is less efficient due

to partial absorption of emitted fluorescence and a smaller phytoplankton optical cross section (*i.e.*, a_{ph}/chl smaller) associated with a greater 'packaging effect' [20]. Another interesting feature of the CASPER fluorescence spectra was the spectral shift of the phytoplankton fluorescence peak at higher chl values. This phenomenon was previously reported based on field measurements [9,34] and is related with a spectral shift to longer wavelengths on L_w and driven by a greater contribution of elastic scattering with respect to chlorophyll fluorescence [9]. Certainly, this spectral shift can not be detected using conventional fluorometers based on a single-wavelength excitation. Thus, we suggest that CASPER and other comparable spectrofluotrometers are a better choice to calibrate in-water and satellite fluorescence-based models of chl.

The relationships found between CASPER-based nFLH and chl samples (field and derived from cultures) are not expected to be substantially influenced by the fluorometric method (*i.e.*, with acidification) or type of fluorometer (excitation wavelength = 436 nm) used in this study. This statement is supported by previous experiments in the SLE during spring 2000 and 2001, and comparing chl measurements based on non-acidification method (chl^{WEL}) [35] or High-Pressure liquid Chromatography (chl^{HPLC}) with fluorometric determinations (chl^{acid} = (0.74 ± 0.05, 1 standard error) chl^{HPLC} +(0.09 ± 0.25), r^2 = 0.80, N = 70; chl^{acid} = 0.88 chl^{WEL} ± 0.03+(0.06 ± 0.15), r^2 = 0.93 N = 70) performed using the same technique and optical instrument (chl^{acid}) [36].

Although a direct relationship was always observed between FLH^{CM} and chl, the fluorescence yield per unit chlorophyll was lower when experiments were performed with phytoplankton cultures. The discrepancy was likely attributed to the greater light levels used in the incubated samples with respect to those characteristic of field measurements. PAR (*i.e.*, photosynthetic available radiation, wavelength = 400–700 nm) above a threshold of $1.0 \cdot 10^{-4}$ mol·quanta·m^{-2}·s^{-1} can be photo-inhibitory and tends to lower fluorescence/chl [27]. Averaged PAR of incubated samples was $3.5 \cdot 10^{-4}$ mol·quanta·m^{-2}·s^{-1} or more than 3-fold greater than theoretical *in situ* estimates computed as <PAR> = PAR(0+)/(H$_{mix}$ K$_{PAR}$) [37], where PAR(0+) is the PAR at noon and incident at the sea surface during 28 September 2011 ($1.04 \cdot 10^{-3}$ mol·quanta·m^{-2}·s^{-1}), H$_{mix}$ is the averaged mixed layer depth (10 m), and K$_{PAR}$ is the lowest vertical light attenuation coefficient for PAR measured in the SLE (1.1 m^{-1}). Therefore, the above calculations suggest potential modifications on fluorescence/chl in phytoplankton cultures due to excessive light.

Variations in fluorescence between experiments due to changes in micronutrients concentration, water temperature, taxonomic differences, and CDOM are anticipated to be secondary due to the following facts. As specified by Turner designs, the variation of acetone-extracted chlorophyll fluorescence due to temperature is 0.3%/°C. This effect may introduce a negligible error on FLH calculation (up to 3%) if we consider a maximum temperature shift of 10 °C between field and lab measurements.

Based on published reports, the phytoplankton culture used in this study (*N. oculata*) has a fluorescence emission spectrum that is comparable to those associated with bacillariophytes (*i.e.*, diatoms) [38]. Thus, since diatoms dominate over the lower St Lawrence Estuary (*i.e.*, where field samples were collected for CASPER comparisons) [39], uncertainties on CASPER fluorescence curves due to phytoplankton composition are likely minor. In general, phytoplankton growth is not nutrient-limited in the SLE [40], thus nutrients should not have a major influence on phytoplankton fluorescence in our experiments.

The linear behavior between chl and FLH^{CM} variations seemed to contradict empirical and theoretical parameterizations reported by other studies [9,20,33]. However, we attribute this deviation to the lack of 'packaging effect' and re-absorption of photons as a function of chl in the phytoplankton culture experiments. As chl increases, the a_{ph}* tends to decrease and re-absorption of photons tends to increase creating a saturation plateau on fluorescence values [20, 27]. This phenomenon did not occur in our phytoplankton cultures since we worked with diluted samples (*i.e.*, same abundance per volume) and phytoplankton cells were exposed to similar light conditions during the incubation.

4.2. Coherence between chl^{CASPER} and other Chlorophyll Indices

Although chl^{CASPER} and chl^{SM} were both based on fluorescence line height changes, the empirical model developed with MODIS-Aqua and shipboard measurements only corresponded with CASPER estimates in 34% of the cases (Figure 4(A)). In addition, both variables did not follow a 1:1 relationship. This is not surprising given three main reasons: (1) the increase in fluorescence variability in field samples with respect to laboratory measurements, due mainly to changes on a_{ph}* (Equation (2) in [20]), (2) differences between spectral bands used in MODIS-Aqua and CASPER-MODIS models to compute FLH (Figure 1 in [20]), and (3) bias attributed to spectral changes in excitation light source (*i.e.*, laser in CASPER *vs.* sun-induced in MODIS or MERIS) and receiver's differences (*i.e.*, detector response of CASPER *vs.* satellite sensors). As highlighted in Figure 4(C), a variation in chl^{CASPER} was followed by a comparable rate of change of chl^{GSM} even though the regression intercept suggested a 'residual' pigment as computed by the GSM model when chl^{CASPER} was 0 mg·m^{-3}. This pigment offset was attributed to a greater CDOM interference on chl^{GSM} with respect to chl^{CASPER}. CDOM is a dominant optical component that is responsible for absorbing most of the blue light in the SLE [7]. Thus, in CDOM-rich waters, the total light absorption at 443 nm (*i.e.*, maximum absorption peak for chlorophyll) increases, resulting in an overestimation of chl when this pigment is measured using remote sensing reflectance ratios. To illustrate this effect we have that chl is inversely proportional to R1 = $R_{rs}(443)/R_{rs}(550)$ = $(a(550) b_b(443))/(a(443) b_b(550))$, where a and b_b are total absorption (*i.e.*, water + particulates + CDOM) and backscattering coefficients at the corresponding wavelengths. Therefore, if chl and $b_b(443)/b_b(550)$ are constant, and magnitude of $a_{CDOM}(443)$ is larger, 1/R1 becomes smaller and chl is higher.

Why did chl^{oc3} and chl^{NN} not have a good correspondence with chl^{CASPER}? Unlike the other global products of chl, the performance of chl^{oc3} is highly influenced by CDOM interference since it uses less spectral information than the other models to tease out the optical contribution of phytoplankton from that associated with CDOM. The lack of covariability between chl^{NN} and chl^{CASPER} in the SLE is not surprising since chl^{NN} was originally developed with specific neural network coefficients obtained from European coastal waters. In fact, this neural network is initialized with TSM measurements made over the North Sea and the Baltic Sea. Thus, a large uncertainty on chl^{NN} can be expected between the SLE and European coastal environments due to changes on SPM optical properties between different water bodies and associated to variations on organic content and size distribution of particulates. As shown in Table 2, a hyperbolic function was a more accurate regression model for relating chl^{CASPER} with global chl products. These results support the non-linear behavior between chl and fluorescence, and corroborate semi-empirical relationships suggested by Gower's and Gilerson's studies [9,20].

4.3. Spatial Distribution of Spaceborne Chl Indices

The use of discrete shipboard measurements for characterizing large scale patterns of phytoplankton in surface waters of the Saint Lawrence Estuary may be misleading if oceanographic surveys are inadequate in terms of spatial coverage or density of sampling locations. Likewise, satellite measurements based on L_w may not be useful for mapping horizontal variations of chlorophyll in this environment if global ocean color products (e.g., chl^{NN}) are not locally validated. In that regard, we demonstrated the superior ability of spaceborne FLH measurements for deriving more realistic distributions of chl in SLE waters.

Consistent with '*in situ*' historical fluorescence measurements [11], chl^{CASPER} presented maximum values (*i.e.*, >10 mg·m^{-3}) in three areas of the Estuary: north of Aux-Coudres Island in the upper Estuary (47.7°N, 69.9°W, I), nearby Forestville city (48.55°N, 69.145°W, II), and the Manicougan Peninsula (49.07°N, 68.19°W, III) in the north shore of the lower Estuary. These high chl spots are likely created by downstream advection and resuspension of benthic diatoms (I) [41], divergence fronts (II) [42], and river plumes (III) [43]. Unlike other studies, the analysis of chl^{CASPER} fields during September 28 also suggested relatively high pigment concentrations in the proximity of the Saguenay Fjord entrance and along the opposite coast extending to 48.49°N, 68.55°W. These sites correspond with major tidal flats environments (e.g., Bay Sainte-Anne, Berte Island, Figure 1) and an active transport of sediments including attached microalgae [41].

Although chl^{CASPER} and chl^{SM} are more suitable metrics for describing variations of chlorophyll in the SLE with respect to global ocean color products, the interpretation of geographic variability of chlorophyll based on satellite fluorescence may be compromised if one or more of the following factors play an important role altering FLH: (1) inaccurate atmospheric correction, (2) modified phytoplankton physiological parameters affecting quantum yield of fluorescence (ΦF) and/or $a_{ph}*$, and (3) influence of high concentration of detritus and/or CDOM on fluorescence excitation/emission spectra. Regarding the first factor, we compared MERIS top-of-the atmosphere (TOA) reflectance measurements over the SLE with simulated TOA values computed using a radiative transfer model (6SV, [44]) and local meteorological information obtained from AERONET and airport weather stations located at Mont Joli and Quebec City. During 28 September 2011, measured TOA radiance due to aerosols accounted for 20 and 40% of total radiance at λ_S and λ_L, respectively. Satellite-derived optical thickness of aerosols at 869 nm, the most important uncertainty in atmospheric models, was relatively small and invariable (0.03 to 0.08) suggesting relatively low concentration of aerosols over the study area. Preliminary results show a maximum bias of 25% (29.9% at λ_S, 20.8% at λ_L) between simulated and measured TOA reflectance. Thus, we conclude that atmospheric correction of ocean color products used in this study was satisfactory and its uncertainty is relatively small with respect to the nFLH variation observed in the SLE (several orders of magnitude, see Figures 6(C,D) and 7(C,D)). However, satellite measurements of nFLH under turbid atmospheres and high solar zenith angles are expected to be more inaccurate by increasing the detection limit of chl retrievals up to 2.6-fold [10].

With reference to the second factor, nFLH is expected to change in a direct way with respect ΦF and $a_{ph}*$ (Equation (2) in [27]). Previous investigations have shown that the magnitude of $a_{ph}*$ during April–May 2000 and 2001 cruises in the SLE varied between 2.8 and 6.4-fold, respectively [45]. Therefore, in our study area, the impact of this variability for satellite chlorophyll fluorescence should be

secondary. The influence of ΦF on nFLH is more difficult to assess over the SLE since there are no direct *in situ* measurements of ΦF (e.g., based on fast rate pulse fluorometers). However, no major changes on ΦF are expected in our study area given the lack of nutrient-limiting conditions for phytoplankton growth [43]. Based on radiative transfer simulations, Gilerson *et al.* [9] concluded that ΦF is relatively constant and equal to 1% in coastal waters having chl values ranging from 1 to 50 mg·m^{-3}.

Reduction in nFLH due to non-photochemical quenching may occur if phytoplankton cells are exposed to damaging solar radiation levels [27]. However, mid-day fluorescence depression due to photo-inhibition is unlikely in our satellite-derived nFLH values (see Section 4.1) unless waters are relatively shallow (bottom depth <10 m) and clear (K_{PAR} < 1 m^{-1}). These environments are spatially constrained as they only represent less than 10% of the SLE surface area [46]. The third factor affecting nFLH mainly relates to the interference exerted by dominant optical water constituents other than pigmented particulates. The analysis of relationships between the CDM and nFLH for different regions of the SLE did not support a hypothetical suppression of phytoplankton fluorescence due to CDOM-mediated spectral overlap of chlorophyll excitation wavelengths as proposed by other studies [9]. This apparent discrepancy was probably attributed to the larger effect of detritus-derived elastic scattering with respect to CDOM light attenuation on nFLH variability.

In general, nFLH and TSM were directly related over different waters of the SLE (Figure 7(D)). However, this correspondence varied for different TSM intervals (m = 0.028 for TSM = 0.5 and 2 g·m^{-3} and m = 0 for TSM = 2.5 to 20 g·m^{-3}). TSM includes a variable contribution of algal particulates, thus we suggest that nFLH variability is dominated by microalgae at lower TSM values (e.g., south shore and upwelling regions). Conversely, the leveling off of nFLH at higher TSM values could be interpreted as an increase in detritus mass with respect to microalgae (e.g., MTZ and north shore). The aforementioned impact of detritus on chlorophyll fluorescence peak and FLH has been investigated by Gilerson *et al.* [9,33] who showed that chl explains one-third of FLH variability when concentrations of non-algal particulates (NAP) are relatively low (<2 g·m^{-3}). However, FLH may not be an accurate proxy for chl when NAP concentrations are above 2 g·m^{-3} and becomes an useless index at NAP concentrations above 10 g·m^{-3} due to the overwhelming contribution of elastic scattering (>95%) with respect to fluorescence. In this study, we estimate a NAP range between 0.5 (e.g., upwelling and south shore) and 20 g·m^{-3} (e.g., MTZ and north shore) [7], thus our chl^{CASPER} index may be used in the SLE only in those locations characterized by relatively low to moderate turbidity and having concentrations of total suspended particulate matter below 13 g·m^{-3}.

5. Conclusions

Comparisons between satellite and field data showed that nFLH is a very good indicator of chl in surface waters of the SLE (e.g., r^2 = 0.89 in Figure 3) characterized by relatively low to moderate detritus concentrations (*i.e.*, ≤10 g·m^{-3}). In addition, we found that alternative remote sensing proxies of chl based on elastic scattering and light absorption coefficient variations may present large uncertainties (up to 48, 134 and 860-fold for chl^{GSM}, chl^{oc3} and chl^{NN}, respectively) with respect to fluorescence-based estimates. Global NASA and ESA chl products examined here mainly failed due to the high interference of CDOM at relatively short wavelengths (<400 nm) and the local variability of water optical properties.

Although more comparisons between CASPER-derived fluorescense, L_w, and chl are needed to make chl^{CASPER} an absolute proxy for chlorophyll, we suggest the use of spectrofluorometry to validate remote sensing models of chl in dynamic and optically complex waters such as those corresponding to the SLE. Mini-spectrofluorometers like CASPER are ideal instruments for validating satellite-derived chl models since they allow cheap (*i.e.*, <1 US dollar per sample), fast (*i.e.*, <1 s) and accurate (*i.e.*, ±0.1%) chl measurements at very high temporal (*i.e.*, seconds) and spatial (*i.e.*, cm) resolution, and over a wide dynamic range (*i.e.*, 0.1 to 400 mg·m^{-3}).

References

1. Legendre, L. The significance of microalgal blooms for fisheries and for the export of particulate organic carbon in oceans. *J. Plankton Res.* **1990**, *12*, 681–699.
2. Fauchot, J.; Saucier, F.J.; Levasseur, M; Roy,S; Zakardjian, B. Wind-driven river plume dynamics and toxic Alexandrium tamarense blooms in the St. Lawrence estuary (Canada): A modeling study. *Harmful Algae* **2008**, *7*, 214–227.
3. Montes-Hugo, M.; Carder, K.; Foy, R.; Cannizzaro, J.; Brown, E.; Pegau, S. Estimating phytoplankton biomass in coastal waters of Alaska using airborne remote sensing. *Remote Sens. Environ.* **2005**, *98*, 481–493.
4. McKee, D.; Cunningham, A.; Dudek, A. Optical water type discrimination and tuning remote sensing band-ratio algortihms: Application to retrieval of chlorophyll and K_d(490) in the Irish and Celtic Seas. *Estuar. Coast. Shelf Sci.* **2007**, *73*, 827–834.
5. Carder, K.; Chen, F.R.; Lee, Z.P.; Hawes, S.K.; Kamykowski, D. Semianalytic Moderate-Resolution Imaging Spectrometer Algorithms for Chlorophyll A and Absorption with bio-optical domains based on nitrate-depletion temperatures. *J. Geoph. Res.-Oceans* **1999**, *104*, 5403–5421.
6. Letelier, R.M.; Abbott, M.R. An analysis of chlorophyll fluorescence algorithms for the Moderate Resolution Imaging Spectrometer (MODIS). *Remote Sens. Environ.* **1996**, *58*, 215–223.
7. Montes-Hugo, M.A.; Mohammadpour, G. Biogeo-optical modeling of SPM in the St Lawrence Estuary. *Can. J. Remote Sens.* **2012**, *38*, 1–13.

8. Gower, J.F.R. *Study of Fluorescence-Based Chlorophyll a Concentration Algorithms for Case 1 and Case 2 Waters*; European Space Agency (ESA), European Space Research and Technology Centre (ESTEC): Noordwijk, The Netherlands, 1999; Contract 12295/97/NL/RE.

9. Gilerson, A.; Zhou J.; Hlaing, S.; Iannou, I.; Schalles, J.; Gross, B.; Moshary, F.; Ahmed, S. Fluorescense component in the reflectance spectra from coastal waters. Dependence on water composition. *Opt. Exp*. **2007**, *15*, 15702–15721.

10. Abbott, M.R.; Letelier, R.M. *Algorithm Theoretical Basis Document. Chlorophyll Fluorescence (MODIS Product Number 20)*; NASA: Pasadena, MD, USA, 1999; p. 42.

11. Nieke, B.; Reuter, R.; Heuermann, R.; Wang, H.; Babin, M.; Therriault, J.C. Light absorption and fluorescence properties of chromophoric dissolved organic matter (CDOM) in the St. Lawrence Estuary (Case 2 waters). *Cont. Shelf Res.* **1997**, *17*, 235–252.

12. D'Anglejan, B.F.; Smith, E.C. Distribution, transport and composition of suspended matter in the St. Lawrence Estuary. *Can. J. Earth Sci*. **1973**, *10*, 1380–1396.

13. Fuentes-Yaco, C.; Vezina, A.F.; Larouche, P; Vigneau, C; Gosselin, M; Levasseur, M. Phytoplankton pigment in the Gulf of St. Lawrence, Canada, as determined by the Coastal Zone Color Scanner. Part 1. Spatio-temporal variability. *Cont. Shelf Res.* **1997**, *17*, 1421–1439.

14. Mucci A.; Starr M.; Gilbert D.; Sundby B. Acidification of the lower St Lawrence Estuary bottom waters. *Atmosphere-Ocean* **2011**, *49*, 206–218.

15. Trees, C.C.; Bidigare, R.R.; Karl, D.M.; Van Heukelem, L. Fluorometric Chlorophyll a: Sampling, Laboratory, Methods and Data Analysis Protocols. In *Ocean Optics Protocols for Satellite Ocean Color Sensor Validation*; Chapter 14, Revision 2; NASA Report; Goddard Space Flight Space Center: Greenbelt, MD, USA, 2000.

16. Colao, F.; Demetrio, E.; Drozdowska, V.; Fiorani, L.; Lazi, V.; Okladnikov, I.. Palucci A. Seawater Dual Fluorescence Analysis during the Arctic Summer 2006 Polish Oceanographic Campaign. In *Proceedings of 3rd EARSel Workshop Remote Sensing of the Coastal Zone*, 7–9 June 2007, Bolzano, Italy.

17. Falkowski, P.G.; Kiefer, D.A. Chlorophyll a fluorescence in phytoplankton: relationship to photosynthesis and biomass. *J. Plankton Res.* **1985**, *7*, 715–731.

18. Neville, R.A.; Gower, J.F.R. Passive remote sensing of phytoplankton via chlorophyll fluorescence. *J. Geophys. Res.* **1977**, *82*, 3487–3493.

19. Borstad, G.A.; Edel, H.R.; Gower, J.F.R.; Hollinger, A.B. *Analysis of Test and Flight Data from the Fluorescence Line Imager*; Can. Spec. Publ. Fish. Aquat. Sci.; Canada Dept. of Fisheries and Oceans: Ottawa, ON, Canada, 1985; Volume 83, p. 48.

20. Gower, J.F.R; Brown, L.; Borstad, G.A. Observation of chlorophyll fluorescence in west coast waters of Canada using the MODIS satellite sensor. *Can. J. Remote Sens*. **2004**, *30*, 17–25.

21. Ocean Color Web. Available online: http://oceancolor.gsfc.nasa.gov/ (accessed on 1 January 2012).

22. GlobColour. Available online: http://hermes.acri.fr/ (accessed on 1 January 2012).

23. O'Reilly, J.E.; Maritorena, S.; Mitchell, B.G.; Siegel, D.A.; Carder, K.L.; Garver, S.A.; Karhu, M.; Garver, S.A; MCClain, S.A. Ocean color algorithms for SeaWiFS. *J. Geoph. Res.* **1998**, *103*, 24937–24953.

24. Maritorena, S.; Siegel, D.A. Consistent merging of satellite ocean color data sets using a bio-optical model. *Remote Sens. Environ.* **2005**, *94*, 429−440.

25. Doerffer, R.; Schiller, H. The MERIS Case 2 algorithm. *Int. J. Remote Sens*. **2007**, *28*, 517–535.

26. Doerffer, R.; Schiller, H. *MAPP Data Products Definition and Algorithm Specification. Algorithm Theoretical Basis Document (ATBD). Regionalized Case II Water Products and Algorithms*; ATBD 1, Report; GKSS Research Center: Hamburg, Germany, 2000; p. 87.

27. Behrenfeld, M.; Westberry, T.K.; Boss, E.S.; O'Malley, R.T.; Siegel, D.A.; Wiggert, J.D.; Franz, B.A.; McClain, C.R.;Feldman, G.C.; Doney, S.C.; Moore, J.K.; Dall'Olmo, G.; Milligan, A.G.; Lima, I; Mahowald, N. Satellite-detected fluorescence reveals global physiology of ocean phytoplankton. *Biogeosciences* **2009**, *6*,779–794.

28. Gordon, H.R.; Clark, D.K. Clear water radiances for atmospheric correction of coastal zone color scanner imagery. *Appl. Opt*. **1981**, *20*, 4175–4180.

29. GlobProject. Available online: http://www.brockmann-consult.de (accessed on 1 January 2012).

30. Windows Image Manager Software. Available online: http://wimsoft.com/ (accessed on 1 January 2012).

31. Sokal, R.R.; Rohlf, F.J. *Biometry*; W.H. Freeman: New York, NY, USA, 1995; p. 498.

32. Pearson, R.K. *Mining Imperfect Data. Dealing with Contamination and Incomplete Records*; Society for Industrial and Applied Mathematics: Philadelphia, PA, USA, 2005; p. 305.

33. Gilerson, A.; Zhou, J.; Hlaing, S.; Iannou, I.; Gross, B.; Moshary, F.; Ahmed, S. Fluorescence component in the reflectance spectra from coastal waters. II. Performance of retrieval algorithms. *Opt. Exp*. **2007**, *16*, 2446–2460.

34. Ahn, Y-H; Shanmugam, P. Derivation and analysis of the fluorescence algorithms to estimate phytoplankton pigment concentration in optically complex coastal waters, *J. Opt. A-Pure Appl. Opt*. **2007**, *9*, 352–362.

35. Welschmeyer, N.A. Fluorometric analysis of chlorophyll a in the presence of chlorophyll b and phaeopigments. *Limnol. Oceanogr*. **1994**, *39*, 1985–1992.

36. Mas S. Le Rôle du Phytoplancton de petite Taille (<20 μm) dans les Variations des Propriétés Optiques des Eaux du Saint-Laurent. Ph.D. Thesis, Université du Québec a Rimouski, Rimouski, QC, Canada, 2008; p. 286.

37. Cloern, J.E.; Grenz, C.; Vidergar-Lucas, L. An empirical model of the phytoplankton chlorophyll: Carbon ratio-the conversion factor between productivity and growth rate. *Limnol. Oceanogr.* **1995**, *40*, 1313–1321.

38. Poryvkina, L.; Babichenko, S.; Leeben, A. Analysis of Phytoplankton Pigments by Excitation Spectra of Fluorescence. In *Proceedings of EARsel-SIG Workshop*, *Lidar Remote Sensing of Land and Sea*, Dresden, Germany, 16–17 June 2000.

39. Roy, S.; Chanut, J.P.; Gosselin, M.; Sime-Ngando, T. Characterization of phytoplankton communities in the lower St Lawrence Estuary using HPLC-detected pigments and cell microscopy. *Mar. Ecol. Progr. Ser*. **1996**, *142*, 55–73.

40. Levasseur, M.; Therriault, J.C.; Legendre, L. Hiercharchid controls of phytoplankton succession by physical factors. *Mar. Ecolo. Progr.Ser*. **1984**, *19*, 211–222.

41. Lucotte, M. Organic carbon isotope ratios and implications for the maximum turbidity zone of the St Lawrence Estuary. *Est. Coast. Shelf Sci*. **1989**, *29*, 293–304.

42. Fortier, L.; Leggett, W.C. A drift study of larval fish survival. *Mar. Ecol. Progr. Ser*. **1985**, *25*, 245–257.

43. Therriault, J.-C.; Levasseur, M. Control of phytoplankton production in the lower St. Lawrence Estuary: Light and freshwater run-off. *Le Nat. Canad.* **1985**, *112*, 77–96.

44. Vermote, E.F.; El Saleous, N.Z.; Justice, C.O. Atmospheric correction of MODIS data in the visible to middle infrared: first results. *Remote Sens. Environ.* **2002**, *83*, 97–111.

45. Roy, S.; Blouin, F.; Jacques, A.; Therriault, J.C. Absorption properties of phytoplankton in the lower Estuary and Gulf of St Lawrence. *Can. J. Fish. Aquat. Sci.* **2008**, *65*, 1721–1737.

46. Montes-Hugo, M., Mohammadpour, G. Uncertainties on satellite-derived SPM estimates due to bottom–reflected light: A case study in the Saint Lawrence Estuary. *Int. J. App. Earth Obs. Geoinf.* **2012**, submitted.